Journal of Medical Robotics Research, Vol. 6, Nos. 1 & 2 (2021) 2140002 (12 pages)

DOI: 10.1142/S2424905X2140002X

Journal of Medical Robotics Research
https://www.worldscientific.com/worldscinet/jmrr

Journal of Medical Robotics Research

Super Resolution for Improved Positioning of an MRI-Guided Spinal Cellular Injection Robot

Daniel Enrique Martinez[*,¶], Waiman Meinhold[*], John Oshinski[†], Ai-Ping Hu[‡], Jun Ueda[§,‖]

[*]*Robotics PhD Program, Georgia Institute of Technology*
North Ave NW, Atlanta GA 30332, USA

[†]*Department of Radiology, Emory University*
201 Dowman Dr, Atlanta GA 30322, USA

[‡]*Intelligent Sustainable Technologies Division*
Georgia Tech Research Institute
640 Strong Street, Atlanta GA 30318, USA

[§]*The George W. Woodruff School of Mechanical Engineering*
Georgia Institute of Technology, North Ave NW, Atlanta GA 30332, USA

This paper presents the development of a magnetic resonance imaging (MRI)-conditional needle positioning robot designed for spinal cellular injection. High-accuracy targeting performance is achieved by the combination of a high precision, parallel-plane, needle-orientation mechanism utilizing linear piezoelectric actuators with an iterative super-resolution (SR) visual navigation algorithm using multi-planar MR imaging. In previous work, the authors have developed an MRI conditional robot with positioning performance exceeding the standard resolution of MRI, rendering the MRI resolution the limit for navigation. This paper further explores the application of SR to images for robot guidance, evaluating positioning performance through simulations and experimentally in benchtop and MRI experiments.

Keywords: Super resolution; magnetic resonance imaging; visual robot guidance; surgical robots; needle steering; cellular therapeutics; spinal cord.

JMRR

1. Introduction

Treatment of degenerative neurological conditions such as spinal cord injury, spinal muscular atrophy, multiple sclerosis, and amyotrophic lateral sclerosis (ALS or Lou Gehrig's disease) has shown promising results using stem cells to provide neural protection, axonal regeneration, and re-myelination (enabling nerve impulses to travel faster). Based on small animal models and limited human trials, the best outcomes are observed when the cells are directly delivered via injection to specific locations within the spinal cord, for example, targeting the ventral horn [1, 2].

Open surgery is the current standard approach which requires invasive removal of the lamina, and the exposure of the spinal cord and injection site for visual location by the surgeon. MRI-based injection is preferable to open surgery because it enables accurate location of injection sites in a minimally invasive manner [1]. However, in the current paradigm, the patient is inserted into the MRI scanner and multi-planar images of the spine along with the device are taken. The patient is removed, the device is manually adjusted to move the needle closer to the target pose, and then the patient is re-inserted and re-imaged. This process is repeated multiple times before final

Received 23 December 2020; Revised 4 March 2021; Accepted 4 April 2021; Published 15 May 2021. Published in JMRR Special Issue: ISMR 2020. Guest Editor: Iulian Ioan Iordachita.
Email Addresses: ¶*dmartinez43@gatech.edu*, ‖*jun.ueda@me.gatech.edu*

needle delivery, such that the patient insert-remove iterations add upwards of 90 min (about one-quarter of the total procedure time) to the cell injection procedure. This manual approach in MRI may lead to significant trauma to the region around the spinal cord and to excessive MRI scanner and operating room time. In addition, the highly manual procedure can lead to inaccurate delivery of cells to the targeted locations.

Recent work in cellular therapeutics has indicated that the ventral horn of the spinal cord is a potentially valuable primary target in the mitigation of many conditions. It is critical that the cellular material is delivered directly to the site, with minimal targeting error, as cells injected into white matter are likely ineffective [3]. Although the spinal cord is approximately 12 mm in diameter [4], the ventral horn is much smaller, with a cross sectional area near 1 mm^2. To target such a small area effectively with the needle tip, the distal needle posing accuracy requirement must exceed 1 mm (i.e. be better than 1 mm precision), which is comparable to the resolution of most clinical MR imaging.

To achieve MRI guided intraspinal injection, the previous research of the authors has developed a direct drive parallel plane piezoelectric needle positioning robot named the Automated Spinal Precision Injection Needle positioning robot (AutoSPINe) [5, 6]. The proposed MRI visual feedback schematic is shown in Fig. 1. The ability to accurately position and orient the needle by using an automated device within the MRI scanner would have clear clinical benefits. The MRI modality enables simultaneous visualization of both internal anatomical structures as well as contrasting landmarks (fiducials) placed on a robot. Robotic needle positioning in an MRI setting, when compared to manual methods, can potentially lead to significant reductions in the total injection procedure time.

The MRI scanner environment presents two major challenges for the robotic solution to overcome: (1) mechanical design and (2) image-guided navigation. In [5], the design, fabrication, and initial evaluation of needle positioning performance of the AutoSPINe robot have been presented. The robot adopted linear piezoelectric motors to directly drive a parallel plane positioning mechanism. Both accuracy and repeatability of the robot were characterized. It was reported that AutoSPINe was capable of repeatability below 51 μm. Needle endpoint error was limited by imaging modality, but is validated to 156 μm. In [6], the application of super resolution (SR) technique was first proposed for image resolution enhancement. Unlike common MRI SR techniques that usually seek to improve human interpretation of image data for diagnostics, the proposed SR concept aims to improve the positioning performance of the AutoSPINe.

Although promising results were presented in [5, 6], factors limiting the performance were not clearly isolated. SR based on open-loop sub-pixel shifts does not increase the imaging resolution of the target (ventral horn). Nevertheless, the overall injection performance is expected to improve compared with the use of native resolution images for both the robot and target. This issue will be quantified and evaluated in a parameter study. In addition, limited mechanical tolerances of the needle guide would reduce the end-point precision; however, MR imaging resolution was insufficient to investigate this issue. In this paper, to imitate the MRI procedure in the laboratory, a new experimental set-up is developed with imaging systems capable of higher

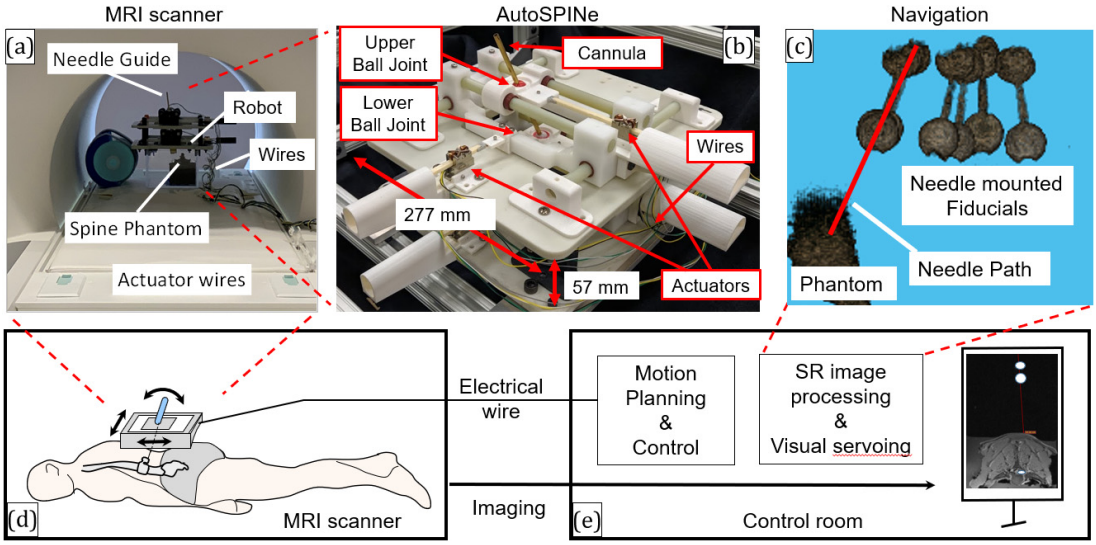

Fig. 1. Needle injection procedure in MRI. (a) shows robot in MRI bore, (b) shows robot dimensions, (c) shows example MRI image with plotted trajectory, (d) shows robot mounted on patient diagram and (e) shows control procedures.

resolution than typical clinical MRI, and sensors that exceed the resolution of the imaging systems.

This paper is organized as follows: Sec. 2 provides an overview of SR-based robot guidance and its challenges. Section 3 describes the design and kinematics of the AutoSPINe. Section 4 explains the concept of SR visual navigation of the AutoSPINe in detail. Simulation results verify the improvement of positioning performance using SR imaging of the marker on the robot. Section 5 evaluates the full four DOF positioning capabilities of the AutoSPINe using a new experimental set-up and compares the results with needle puncture results in MRI. Section 6 discusses findings, limitations and future work. Section 7 provides concluding remarks.

2. Super Resolution of MR Imaging for Robot Guidance

Super resolution enhancement of images was first developed by using several frames of a video sequence [7]. Since then it has become an increasingly popular area of research with many different algorithms being developed, including more recently the use of deep learning models [8]. The goal of SR is to regain some of the information lost in the image capturing process. There exist interpolation and deep learning based methods for single images, as well as methods for multiple images with known differences. These algorithms have been used for improving the visual quality of images for visual inspection, as well as for robotic applications via object detection [9].

SR algorithms have been particularly of interest in medical imaging due to the limited resolution of the imaging sensors compared to RGB cameras, and the need to visualize small features. Imaging parameters such as resolution and speed can often be adjusted to balance clinical factors such as the size of the tissue of interest and available system time. Depending on the imaging method, the resolution can be adjusted based on several factors to balance speed and resolution requirements. For example, a higher MRI resolution can be obtained with a longer scan time, but the longer scan time on a moving tissue can lead to image artifacts. SR has also been applied to images where a fast acquisition time is needed to minimize the image artifact [10]. Though these applications are usually used for visual inspection of features in the image, such as identifying tumors, white matter, and nerves [11, 12], locating desired features with a higher fidelity is also beneficial for surgical procedures [13].

Robots designed for use in medical imaging environments need to adhere to the constraints placed by the imaging system. MR images can suffer distortions and reduced SNR from the presence of certain metals in the area. To retain image quality, the workflow must be designed so that the robot is used outside of the MRI, or the robot must be designed to be MRI safe/conditional and minimize interference with the image acquisition. Workarounds include shielding electronics and wires, using only MRI safe materials, using actuators that can be positioned remotely but transfer the movement to the imaged area via cables or pneumatic systems, and the use of MRI safe actuators. Because of these design constraints, there are limited number of MRI safe robots with positioning capability past resolution of MRI [14]. However, in previous work the authors developed an MRI conditional robot with positioning capability exceeding MRI resolution [5], opening the possibility of application of SR algorithms by controlled physical shifts.

In previous work, the authors used the developed robot to introduce known sub pixel spatial shifts for SR reconstruction of images. The SR images were used for 2-axis guidance of the robot to a desired target position denoted in the image. Comparison between repeatability of guidance using NR (native resolution) images and super resolution images in both the MRI setting and bench top setting demonstrated improvement of about 30% in both cases. Having proven this method to be effective for improving positioning performance, this paper seeks to explore how to implement SR robot guidance for four DOF positioning of the robot and to quantify the improvement in four DOF positioning through numerical and experimental methods.

3. AutoSPINe

3.1. *Design*

To achieve both a large range of motion and high degree-of-freedom (DOF) positioning, serial-link mechanisms with a rotary actuator placed at each of the revolute joints are widely used. However, this type of serial chain structure in general tends to lose rigidity and accumulate joint-level positioning errors towards the end-point, resulting in large mechanisms. Backlash and play in gears to drive revolute joints are common issues [15]. Cable-driven mechanisms [16] can place actuators on a base structure and make the link mechanism lighter and more compact, but flexibility of cables limits end-point positioning precision.

In this paper, a direct-drive parallel plane mechanism (D^2P^2) was adopted as shown in Fig. 2(a) [17]. Each plane is a planar x–y positioning mechanism, positioning a ball joint at the center of the stage, driven by orthogonally located linear piezoelectric actuators (PIEZO LEGS, Micromo, Clearwater FL, USA) as shown in Fig. 2(b). The upper and lower ball joints can move independently, controlling fourth DOF of the needle guide. The fifth DOF, i.e. needle depth, is controlled by the surgeon inserting the needle into the cannula. The sixth DOF, i.e. needle

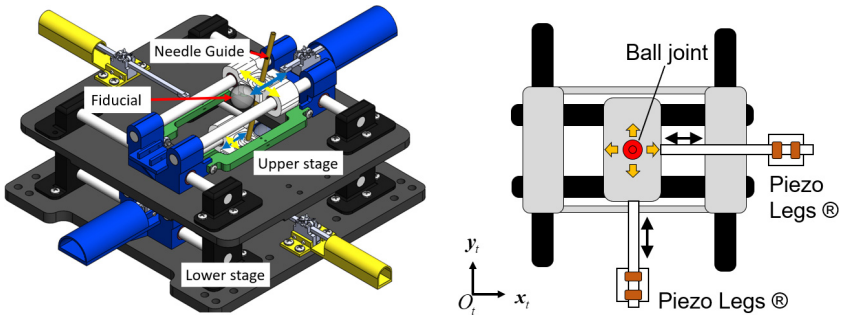

(a) (b)

Fig. 2. The AutoSPINe Robot. (a) CAD drawing of the direct-drive parallel plane mechanism and (b) X–Y linear stage driven by linear piezoelectric actuators. The bottom x–y stage is functionally identical to the upper stage.

rotation, is controlled by the surgeon as well, but the needle angle is irrelevant for this procedure. Because the actual distance between the ball joints is dependent on the orientation, the cannula is fixed in the lower joint, while the upper joint allows the cannula to slide through the center of the ball joint. MRI viability of this robot was verified and reported in [17].

Forward kinematics is presented to represent the needle guide position in the absolute coordinate frame using ball joint positions in the planar coordinate frames fixed to individual x–y stages. Let ${}^{t}\boldsymbol{p}_{\mathrm{BT}} = \begin{bmatrix} x_t \\ y_t \end{bmatrix}$ be the ball position of the top x–y stage with respect to the coordinate frame fixed to it as shown in Fig. 3. Similarity, let ${}^{b}\boldsymbol{p}_{\mathrm{BB}} = \begin{bmatrix} x_b \\ y_b \end{bmatrix}$ be the ball position of the bottom x–y stage. Defining ${}^{t}\boldsymbol{P}_{\mathrm{BT}} = \begin{bmatrix} {}^{t}\boldsymbol{p}_{\mathrm{BT}} \\ 1 \end{bmatrix}$ and ${}^{b}\boldsymbol{P}_{\mathrm{BB}} = \begin{bmatrix} {}^{b}\boldsymbol{p}_{\mathrm{BB}} \\ 1 \end{bmatrix}$, homogeneous transformation, ${}^{0}\boldsymbol{P}_{\mathrm{BT}} = {}^{0}\boldsymbol{T}_{t}\,{}^{t}\boldsymbol{P}_{\mathrm{BT}}$ and ${}^{0}\boldsymbol{P}_{\mathrm{BB}} = {}^{0}\boldsymbol{T}_{t}\,{}^{t}\boldsymbol{P}_{\mathrm{BB}}$ provides the ball positions with respect to the base coordinate frame $\sum_0$ where ${}^{0}\boldsymbol{T}_{t}$ and ${}^{0}\boldsymbol{T}_{b}$ are homogeneous transformation matrices. Note that without the loss of generality, the x–y planes of $\sum_t$ and $\sum_b$ can be assumed parallel to each other to simplify the kinematic representation.

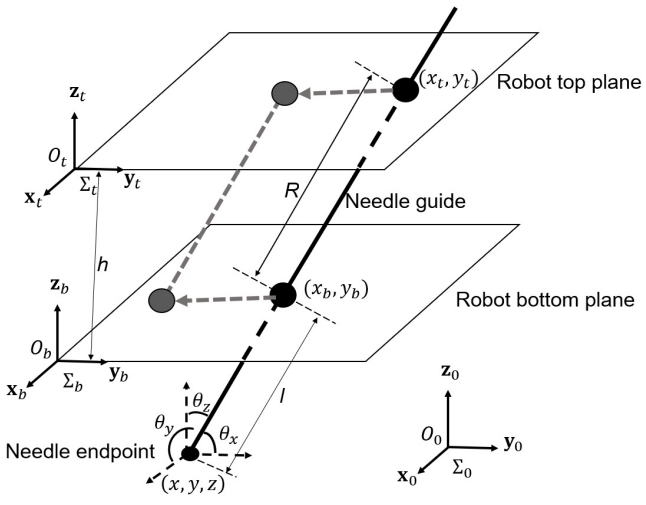

Fig. 3. AutoSPINe kinematics.

3.2. *Measurement of fiducial markers and needle positioning*

Imaging of two fiducial markers attached to the needle guide enables detection of the four DOF position and orientation. The spherical exterior of the fiducial markers makes their outer diameter appear as circles in the MRI regardless of their orientation image slice. Running a circle detection algorithm on an image slice with the fiducial marker visible returns the location of the fiducial marker in the image. The four DOF position and orientation can then be calculated from the location of the two markers. Measurement of ${}^{0}\boldsymbol{P}_{\mathrm{FU}}$ and ${}^{0}\boldsymbol{P}_{\mathrm{FL}}$ determines the line along with the needle guide. The intersection between this line and each of the x–y planes of $\sum_t$ and $\sum_b$ determines the ball joint position. In Fig. 2(a), fiducials are placed next to the ball joint, which requires the transformation from the guide rod to the fiducial to be known. Note that for the benchtop experiments, the ball joints themselves are used as the fiducial markers, which are concentric with the center of the needle trajectory.

Image Jacobians relate small actuator displacements, Δx_t, Δy_t, Δx_b, Δy_b, and resultant ball joint displacements expressed in the global coordinate frame, $\Delta\,{}^{0}\boldsymbol{P}_{\mathrm{BT}}$ and $\Delta\,{}^{0}\boldsymbol{P}_{\mathrm{BB}}$. Matching ${}^{0}\boldsymbol{P}_{\mathrm{BT}}$ and ${}^{0}\boldsymbol{P}_{\mathrm{BB}}$ with the ones of the desired needle position, ${}^{0}\boldsymbol{P}_{\mathrm{BT}d}$ and ${}^{0}\boldsymbol{P}_{\mathrm{BB}d}$, solves the inverse kinematics. Note that the X–Y stages can be operated independently from each other. The solution is unique as long as ${}^{0}\boldsymbol{P}_{\mathrm{BT}}$ and ${}^{0}\boldsymbol{P}_{\mathrm{BB}}$ exist, i.e. unless the needle is not completely orthogonal to the parallel planes. Note the robot has no encoders to measure the position of the robot through forward kinematics, and instead the loop is closed through visual feedback. Use of image Jacobians allow for the control and kinematics to solely be done in the global frame defined by the imaging modality. In general, image-guided needle positioning is performed in an iterative fashion as illustrated in Fig. 4.

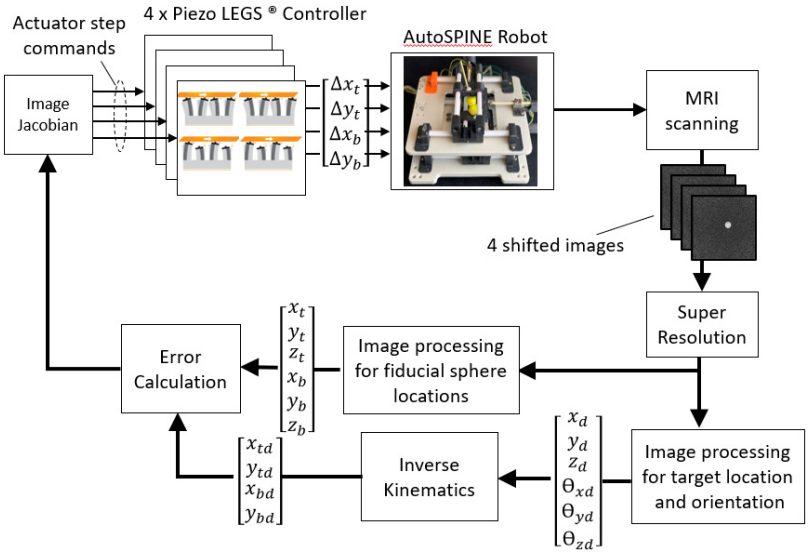

Fig. 4. SR MRI guided needle positioning system diagram.

4. Visual Robot Guidance with Super-Resolution MRI

4.1. *Generating sub-pixel spatial shifts in MRI*

SR imaging technique processes multiple images with known sub-pixel spatial shifts, typically introduced by moving the camera or the object of interest in the scene, and reconstructs a new image that has a higher resolution than that of the original images. Usually a super-resolution image is produced by numerically solving a cost optimization problem [7]. When it comes to resolution enhancement of MRI images, there is a technical barrier to introduction of sub-pixel displacements in the target object. This requires highly precise positioning usable in a MRI scanner. Note that given the specific architecture of MRI, moving the image acquisition component is not an option. The FOV of the MRI image can be changed, and FOV shifts have been used to enhance resolution in the inter-slice direction [18], but in-plane super resolution is generally regarded to be fundamentally impossible without introducing physical shifts of objects in the scene [19]. Natural movement of imaged subject has been used as the spatial shifts by estimating the motion [10], but registration accuracy of this movement is crucial to quality of the SR reconstruction [20].

Performance metrics for the improvement of SR images are usually obtained by comparing an SR image created from simulated low resolution images to the original "ground truth" image the low resolution images were generated from [21]. This is the case because the goal of SR is to regain some of the information lost in the image capturing process, so by simulating that process to generate lower resolution images, and then using SR to reconstruct an image the same size as the original, the SR image can be directly compared to the original image. Measures such as signal to noise ratio and mean square error are used to determine the similarity to the ground truth image, and the reduction of noise in the image. By these methods, the improvement in image quality past the native resolution of the imaging sensor cannot be evaluated by comparison because the original images do not have more information about the ground truth. In this case, we need to compare with more accurate measurements of the scene or metrics specific to the application of the images. For example, In [9], edge and corner detection is evaluated between the NR and SR images because it is the desirable factor for self-localization. Therefore, the method by which to evaluate the improvement of SR algorithms must be designed dependent on the use of the images, and the need for a ground truth image to compare can be eliminated as well.

The application this paper explores is robot positioning in MRI to a desired target position denoted by a clinician. The target position and trajectory are determined by the clinician from the native resolution MRI images, and the fiducial markers on the robot are used to obtain robot position and guide the robot. SR images of the robot will be used to improve the spatial knowledge of the robot for improved positioning, so the key metric is the accuracy of locating the fiducial markers on the robot. Fiducial markers on the robot in MRI are spherical and appear as circles in the image, so the ability to discern the center point location of the circle in the SR images will be tested.

AutoSPINe operates its needle guide and displaces its fiducial markers at resolutions far better than currently possible MRI imaging resolutions [17]. The sub-pixel shifted MRI images are processed to determine the marker positions beyond MRI resolution and navigate the robot toward the target. The displacements are

introduced by operating one or multiple of the PIEZO LEG actuators. Forward kinematics computes resultant small displacements in the fiducial markers. Note that this operation must be performed in an open-loop fashion as sub-pixel movements are essentially not visible in MRI. An arbitrary trajectory may be used to acquire a set of raw images as long as the displacements are known.

4.2. *Specific imaging procedure*

To compute the image Jacobian five points were used, a central origin point, A 1000 step (about 15 mm) movement in the top *x*-axis, a 1000 step movement in the *y*-axis, a 1000 step movement in the bottom *x*-axis, and a 1000 step movement in the bottom *y*-axis. These points were chosen to isolate each of the top and bottom *x* and *y* actuator movements of the robot. For the SR image targeting, it was determined that repeating the Jacobian procedure with the larger resolution images yielded the same result as scaling the native resolution Jacobian.

To determine the spatial shifts for image reconstruction, coordinate points are generated randomly ranging from -1 to 1 pixels. The first point is where the first image is taken and is considered the origin point for the following coordinates. The movement in steps required to reach each of the random points is calculated by subtracting each point from the previous point and multiplying the difference by the inverse of the image Jacobian. The generated shifts will be stored in the offset matrix $\boldsymbol{M}_k$ for each of N images $(k = 1, \ldots, N)$.

The SR image is reconstructed using gradient descent optimization to minimize the error between the native resolution images, $\boldsymbol{I}_k$ $(k = 1, \ldots, N)$, and the current best guess of the SR image to iteratively update the best guess of the SR image:

$$\hat{\boldsymbol{X}} = \underset{\mathbf{X}}{\operatorname{argmin}} \left(\sum_{k=1}^{N} \|\boldsymbol{D}_k \boldsymbol{B}_k \boldsymbol{M}_k \boldsymbol{X} - \boldsymbol{I}_k\|_2^2 \right), \qquad (1)$$

where $\boldsymbol{B}_k$ is the blur matrix and $\boldsymbol{D}_k$ is the down-sampling matrix. This reconstruction was performed by an example code based on the IBP algorithm [22]. Stopping criterion is 100 iterations or when mean square error is below 0.01% of the mean square error before optimization.

For the experimental validation presented in later sections, four images $(N = 4)$ were collected to double the resolution of the original images. Figure 5 shows the four images acquired with a vector arrow representing the spatial shift applied in each image with respect to the first image. After the fourth image is taken, the Auto-SPINe is returned to the first point and the SR image is reconstructed.

4.3. *Simulation*

In clinical situations targeting the ventral horn of the spinal cord, the target object cannot be shifted by the robot, therefore while the information collected of the controlled robot can be improved, the target is limited by the typical MRI resolution. A simulation study was designed to test the hypothesis that using SR images of the robot will still lead to improved positioning despite using low/native resolution images of target.

To simulate the loss of information in the image capturing process, an image of a circle was created at a very high resolution (5000×5000 pixels) with a known center point as the ground truth. To create the lower resolution images, a Gaussian blur was applied, the image was down scaled to desired resolution, and noise was added. As shown in Fig. 6, This process allows us to generate different size images from the same data loss model, allowing us to compare SR images to natively higher resolution images that have lost less information from the image capturing process compared to the smaller images. The image sizes used in the simulation and their labels are outlined in Table 1. MATLAB circle

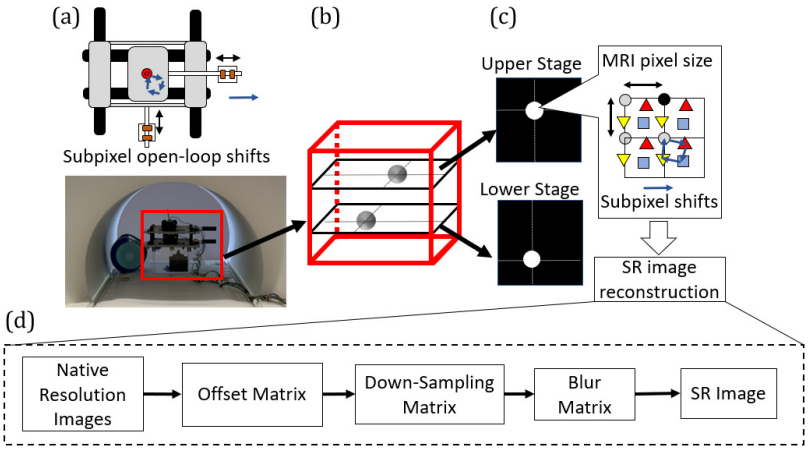

Fig. 5. SR image process in MRI. (a) shows representation of robot in MRI, (b) shows position of ball joints in slices of MRI image, (c) shows subpixel shifts in four images and (d) represents the SR reconstruction algorithm.

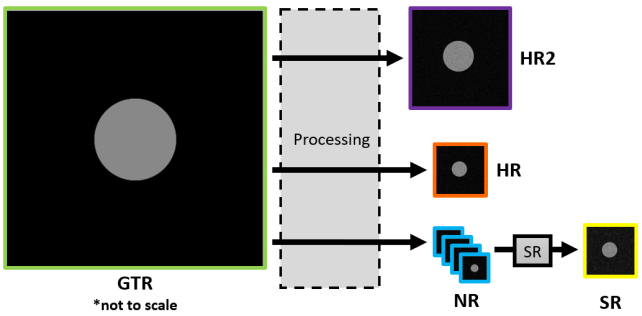

Fig. 6. Generation of different image categories for simulation. All pictures relatively scaled except GTR. "Processing" represents down scaling, blur, and noise. Note that generation of 4 NR images for SR requires 4 separate GTR images (not shown).

Table 1. Size definitions.

Label	Size (pixels)
Native Resolution (NR)	128×128
Super Resolution (SR)	256×256
High Resolution (HR)	256×256
Double High Resolution (HR2)	512×512
Ground Truth Resolution (GTR)	5000×5000

finding function, imfindcircles, which uses hough transforms method, was used to detect markers in images and MRI image slices. The center point position and radius of the markers were retrieved from this method.

Repeating this process several times yields a slightly different image due to the generation of noise. Figure 7 shows the calculated centroid of the circle across 50 images generated at the same center point for NR, SR, and HR images. SR outperformed NR by 61% (MSE 3.12 and 8.01, $p < 0.0001$) and performed 7% better than HR (MSE 3.12 and 3.37, $p < 1$).

NR, SR, HR, HR2, and GTR images of a circle in an arbitrary position were created to represent the controlled robot, with multiple shifted images generated for the SR cases. Standard image processing methods for improving recognition of shapes was applied, namely, binarizing the images through value thresholding, dilation, and erosion. Circle detection was then performed by calculating the centroid of the circles to find the estimated target center point position and robot center point position. The error between the detected current robot position and detected target position was added to the detected current robot position to determine the desired update position. An image of a circle at the desired update position in the respective resolution was generated mimicking the robot movement after an update to the target position. This process was repeated until the norm of error was below 1 pixel (in the respective resolution), and final error was calculated from ground truth position of target center point. This procedure for the SR case is outlined in Table 2.

For the SR, HR, HR2, and GTR cases, the center point of the "native resolution" target image was scaled to correspond to equivalent value in the respective pixel coordinates for each different resolution. For the GTR case the images used to represent the robot were generated with the same process as the NR, HR, and HR2 images but without down scaling.

The results of this simulation for 1000 trials are shown in Fig. 8, with all errors scaled to GTR pixel sizes, and show the GTR method performs best, with a RMS final error across 20 trials of 0.28 pixels. The mean final errors are plotted in Fig. 8 for visibility. The SR method performed 62% better than the NR method, with an RMS of 2.64 and 7.02, respectively ($p < 0.0001$). The SR method also performed 10% better than the High Resolution Images (RMS 2.64 and 2.96, $p < 0.0001$). As expected the trend continues with the Double High Resolution Trials exhibiting an RMS 50% better than the High Resolution Trials (RMS 1.47 and 2.96, $p < 0.0001$). These simulations clearly show that SR applied to the robot images can be used to achieve better performance than the native imaging resolution even when the target images are NR. The results also show promise that SR can achieve similar or even better performance than images double the resolution of the native imaging resolution, and that the higher the resolution of the images used, the better the positioning accuracy will be.

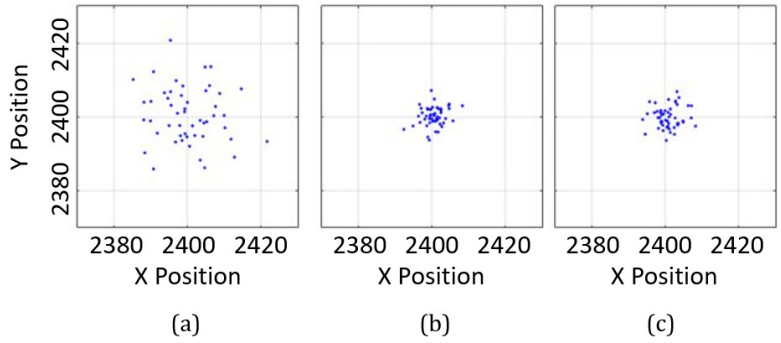

Fig. 7. Detected center points of circle across 50 trials in (a) low resolution, (b) super resolution and (c) high resolution (in pixels).

Table 2. Workflow of numerical analysis.

Step	Description
1	Create 5000 × 5000 pixel image of target circle.
2	Apply blur, downscale, and add noise to image for native resolution target image.
3	Find center point of target circle in generated NR image.
4	Create 5000 × 5000 pixel image of robot circle.
5	Repeat step 2 for NR robot circle image.
6	Repeat steps 4 and 5 to create 3 NR Images.
7	Construct SR image from the 4 NR images and find center point.
8	Scale target center point to equivalent SR size coordinates.
9	Calculate error between robot and target center point.
10	Add error to robot center point for desired center point.
11	Repeat steps 4–7 to generate SR image of robot circle at desired position.
12	Repeat steps 9–11 until norm of error is less than 1 pixel.

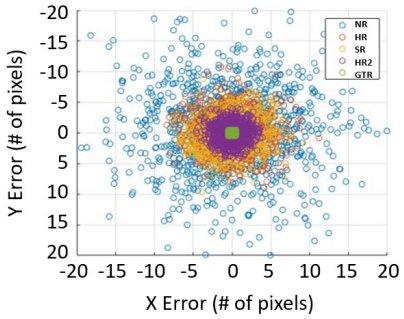

(a)

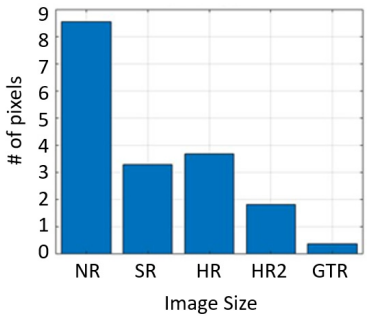

(b)

Fig. 8. Final errors of NR, SR, HR, HR2, and GTR trials. (a) shows the plot of all the final points and (b) shows the mean final error for each trial. Pixel sizes are all in GTR size.

5. Experiments

5.1. *Benchtop experiments*

To measure the accuracy of robot positioning, the target position must be known and measurable. The lack of high-resolution sensors compatible with MRI make it difficult to measure robot position on the micron scale in the MRI setting. However, improvements in positioning accuracy due to the use of enhanced resolution images outside of MRI should apply regardless of the image capturing method.

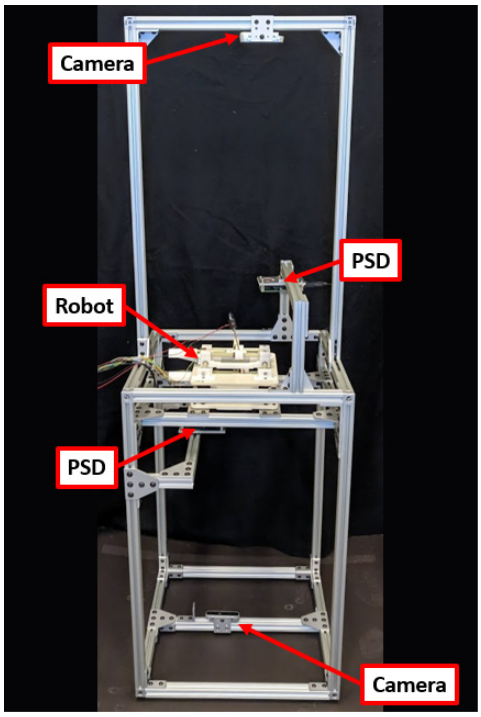

Fig. 9. Benchtop experimental set-up to imitate MRI procedure.

A benchtop experimental set-up as shown in Fig. 9 was developed to measure the robot's full four DOF positioning capabilities by the use of two PSDs (Position Sensitive Detectors, Model S2044, Hamamatsu Corp) positioned above and below the robot facing each other. Fiducial markers were placed directly behind the center of each sensor to mark the line formed between the two sensors as the target position. The robot was mounted on an elevated platform with an RGB camera (Intel Realsense) mounted both above and below the robot to grant visibility of both ball joints and both PSDs. The addition of a bottom camera allows for detection of fiducial markers below the robot as if they were in separate slices of a coronal view of an MRI image. Four fiducials are needed (two for the robot position and two for the target position) in these experiments to measure the 3D position and orientation of the robot and the position and orientation error from the desired position.

The measurement schematic is shown in Fig. 10. Note that the Intel Realsense camera is designed to be capable of measuring not only x and y positions of an object, but also its depth (i.e. z position). Given the geometries of the set-up and the resolution of the camera, the imaging resolution of the markers was approximately 0.9 mm.

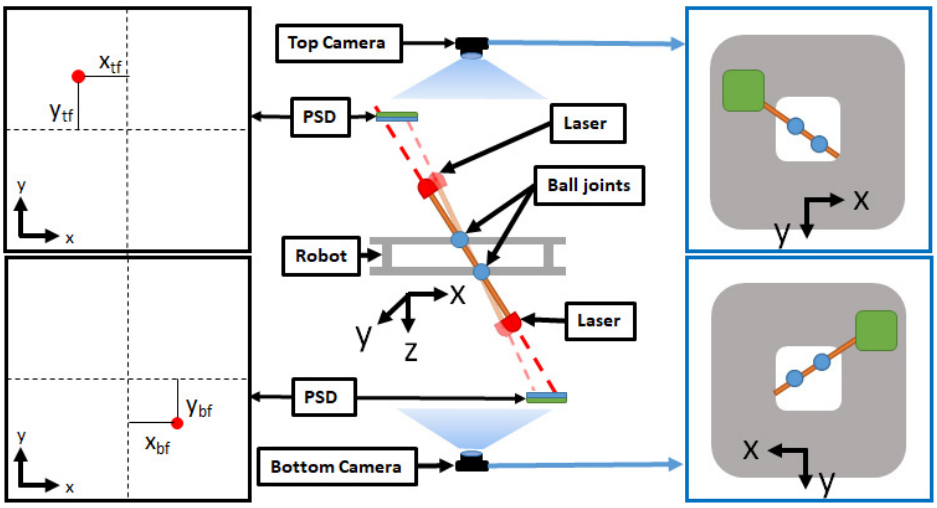

Fig. 10. Side view of the benchtop experimental setup and blown up representation of the image seen by each camera.

The cameras were used for robot positioning following the procedures outlined in Table 3 with two images needed for the robot position as shown in Fig. 11, and the target position being the position that aligns with the two markers mounted on the position sensors. When the target position was achieved within the measurable limit of the cameras, a laser beam was emitted from both ends of the cannula so that it was received by both of the PSDs. The PSDs measure position of a light beam in two axes by calculating the relative intensity of light hitting each of the four quadrants in the sensor. This position is the error from the center of the PSD, which was used as the target position. The two-dimensional errors from each PSD were used to calculate position and orientation error and accuracy. The PSDs used have position resolution of 0.6 μm, allowing us to characterize error with much higher fidelity than the imaging method used for navigation.

Two different desired needle configurations, *A* and *B*, were used for evaluation as shown in Fig. 12. The needle configurations were chosen to avoid visual occlusion that is specific to this camera-based benchtop set-up. Note that visual occlusion is not present in the MRI scanner. For each of the configurations, the top and bottom PSDs were placed such that the emitted laser would be received in the center of the photosensitive area when the needle was correctly positioned. Full four DOF repeatability was evaluated targeting each one of the configurations starting at a configuration away from the desired with a total of 10 trials. Observing positioning errors less than one pixel was used as a stopping criterion that was met in all the trials. Table 4 shows mean and standard deviations of two-dimensional positioning errors with respect to the desired position (i.e. the center of the photosensitive area). Although the positioning repeatability slightly varied between the needle configurations as reported in [5], both the accuracy and precision were comparable to the imaging resolution of the system, indicating that imaging modality is the main limiting factor.

Table 3. Workflow of accuracy experiments.

Step	Description
1	Take images of robot at Jacobian starting position.
2	Move robot and take images to calculate Image Jacobian.
3	Take images of robot at Jacobian arbitrary position.
4	Detect center point of target markers in each image.
5	Calculate target position and orientation.
6	Detect center point of robot markers in each image.
7	Calculate robot position and orientation.
8	Calculate error between robot and target position and orientation.
9	Move robot calculated error and take image(s).
10	Repeat steps 4–9 until norm of error is less than 1 pixel.

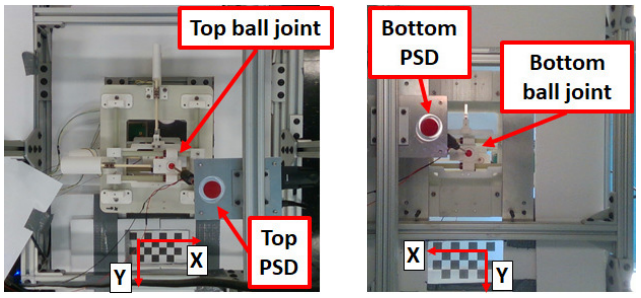

(a) (b)

Fig. 11. Images acquired from top and bottom cameras. (a) Top view, (b) bottom view. The world coordinate frame is defined based on a transparent calibration board seen by the top camera. The bottom camera sees the other side of the calibration board to use the same world coordinate frame.

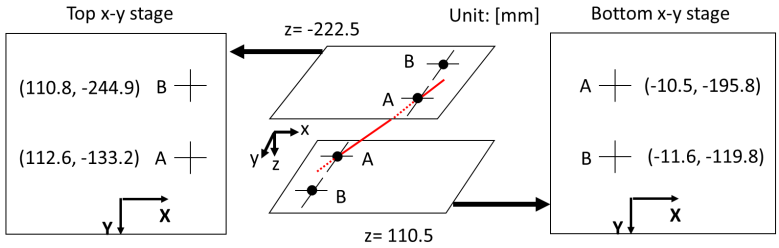

Fig. 12. Test needle configurations *A* and *B* for benchtop experiments.

Table 4. Results of Benchtop needle positioning experiments. Ten trials were performed for each configuration. Mean (STD) are shown in [mm].

Configuration	Top PSD error	Bottom PSD error
A	1.140	1.254
	(1.332)	(1.286)
B	1.288	1.220
	(0.869)	(0.874)

5.2. *MRI validation*

Experiments were carried out in a 3T MRI (Prisma-Fit, Siemens) MRI to confirm the reproducibility of improved positioning upon use of SR images. These experiments were simplified from the procedure described in Sec. 5, with the bottom stage of the robot kept static and only the top plane actuated. A fiducial marker filled with vitamin E was used to visualize the robot in the MRI image, and only one slice of the MRI images was used to calculate the center point of the fiducial in that plane. To ensure the slice of the MRI image goes through the center of the sphere, the slice where the radius of the fiducial is the largest is selected. The fiducial used for this experiment is shown in Fig. 2(a). When the robot reached the desired position set as specific coordinates in the MRI image, a pointed needle was pushed through the guide rod to make a puncture on a sheet of paper mounted below the robot as the target.

The distribution of the punctures on the sheet of paper made from several trials was used to measure the standard deviation, representing the repeatability and precision of the robot positioning. The distance of each point to the group means were measured using a stereo microscope (ModelS6D, Leica, Wetzlar, Germany). Three punctures were made in the NR and SR experiments due to scanner time restrictions precluding collection of a statistically significant sample size. Distributions of punctures are shown in Fig. 13. The standard deviation of the puncture distribution of the SR group was 0.40 mm that was 33% smaller than 0.60 mm of the NR group.

5.3. *MRI safety testing*

MRI suitability of the AutoSPINe was assessed as the image SNR reduction in a Nickel Sulfate solution cylindrical phantom in a 3 Tesla MRI (Siemens Prisma-Fit), and previously reported [5]. Scans were performed under two operating conditions, one with the robot placed above the phantom and one with only the phantom and RF coil in the scanner (control) as shown in Fig. 14. SNRs were calculated to be 244.06 for the control image, and 230.226 with the AutoSPINe. The SNR reduction of 5.7% is well within the 10% reduction criteria for MRI compatibility [23]. Note that SNR during actual motion was not measured as the robot positioning protocol does not necessitate simultaneous actuation and

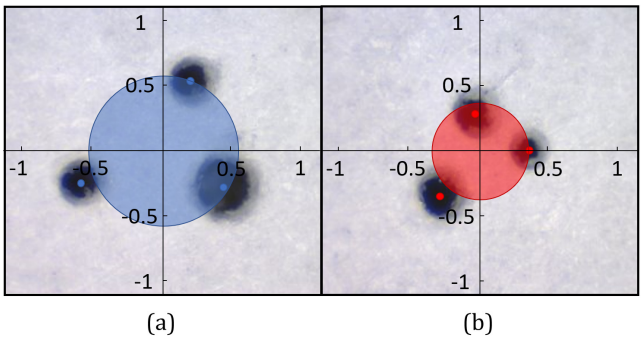

Fig. 13. Puncture distribution of MRI experiments, with the origin as the mean of the points and the large circle representing the standard deviation. (a) shows the NR punctures and (b) shows the SR punctures. Units in mm.

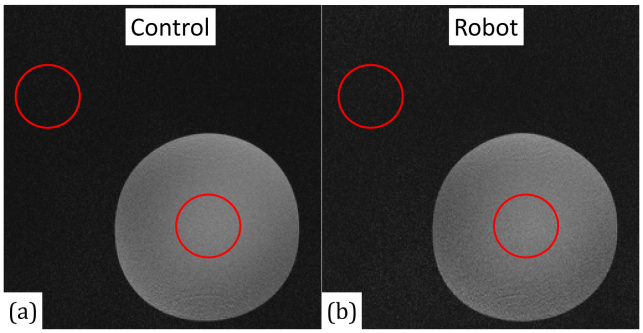

Fig. 14. MRI image quality test results. (a) Control and (b) with the robot.

imaging. To fully verify MRI conditionality, not only image artifact, but also magnetically induced force/torque and radio frequency-induced heating must be measured and evaluated.

6. Discussion

6.1. *Improvement of positioning precision with SR*

The authors reported that the repeatability of the AutoSPINe was not limited by its mechanisms or motion control algorithms, but was essentially limited by imaging modality [5]. When a laser triangulation sensor was used in another benchtop positioning experiments, the AutoSPINe achieved a repeatability of 51 μm. Results in Sec. 5.1 observed the same problem in the full four DOF positioning experiments where the needle positioning was limited by the resolution of the optical camera. The top and bottom ball joints were positioned with errors less than one pixel (approximately 0.9 mm and comparable to general MR imaging resolution) as the stopping criterion.

SR imaging of the needle guide and its sub-pixel positioning can be achieved fully taking advantage of the AutoSPINe's precision mechanism [6]. Section 4.3 confirmed that SR marker detection could improve the positioning precision without SR imaging of the target tissue. To address the latter issue, another emerging SR approach, called single image SR using machine learning [24], may be used for SR imaging of the central horn where the geometries are not fully known in advance.

SR technique enhances image resolution at the cost of increased time of image acquisition. To address this issue, time saving measures, such as using the SR technique only in the final settling phase, or integration with motion control procedures, must be implemented prior to use in a clinical setting.

Note that the needle and needle guide designs were not optimized in this paper. Figure 13 observed increased positioning errors compared with Table 4. This implies that the rigidity and straightness of the needle as well as the sliding tolerance between the needle and needle guide appear to impact the end-point accuracy, which should be addressed in future work.

6.2. *Future cellular therapeutic injection study for the treatment of ALS*

If the proposed robot is successfully introduced into the research of cellular therapeutics, in addition to time-saving benefits, the precision system would facilitate effective usage of cultured cells and quantitative evaluation of their spatial application. One of the most recently concluded trials of stem cells in ALS patients reported adverse effects, [2] primarily related to the required laminectomy and exposure of the spinal cord. The use of a minimally invasive approach would reduce complications and allow for greater patient enrollment, as stringent inclusion criteria could be relaxed, thereby increasing the pace of clinical developments.

In addition to the image time improvements that can and should be made to increase the workflow speed, other practical considerations exist. Patient mounting and sterilization are typical challenges for any precision medical device. Materials and clinical workflows should be designed to enable sterilization of the device prior to use with a patient. Although mounting of the device to the patient is a challenge, the location of the target injection site in the spinal cord is expected to mitigate the motion caused by respiration. Because of the robot guidance method employed, the robot and patient coordinate frames are captured in each image, and patient motion relative to the robot during respiration is expected to be minimal when the robot is mounted to a prone patient.

7. Conclusion

This paper has presented a concept to improve the positioning performance of MRI-guided navigation of a needle positioning robot by applying in-plane super resolution technique. The AutoSPINe robot designed for novel cellular therapeutics was used as an experimental platform. This particular device targets the ventral horn with a cross sectional area near 1 mm^2 that is comparable to the imaging resolution of MRI. Multiple marker images were acquired with open-loop MRI sub-pixel shifts to reconstruct an image with enhanced resolution for needle navigation. Although the presented approach utilized resolution-enhanced images for robot marker imaging, not target tissue imaging, improved positioning precision of 62% was observed in simulation, and 33% in needle puncture experiments in MRI.

Acknowledgments

This work was partially supported by Georgia Tech Interdisciplinary Institute for Robotics and Intelligent Machines Seed Grant Program 2020 and 2021. This material is also based upon work supported by the National Science Foundation under Grant Nos. 1545287 and 1662029. Any opinions, findings, and conclusions or recommendations expressed in this material are those of the author(s) and do not necessarily reflect the views of the National Science Foundation.

References

1. J. J. Lamanna, L. N. Urquia, C. V. Hurtig, J. Gutierrez, C. Anderson, P. Piferi, T. Federici, J. N. Oshinski and N. M. Boulis, Magnetic resonance imaging-guided transplantation of neural stem cells into the porcine spinal cord, *Stereotact. Funct. Neurosurg.* **95**(1) (2017) 60–68.
2. L. Mazzini *et al.*, Results from phase i clinical trial with intraspinal injection of neural stem cells in amyotrophic lateral sclerosis: a long-term outcome, *Stem cells Transl. Med.* **8**(9) (2019) 887–897.
3. M. Janowski, C. Engels, M. Gorelik, A. Lyczek, S. Bernard, J. Bulte and P. Walczak, Survival of neural progenitors allografted into the CNS of immunocompetent recipients is highly dependent on transplantation site, *Cell Transplant.* **23**(2) (2014) 253–262.
4. A. Frostell, R. Hakim, E. P. Thelin, P. Mattsson and M. Svensson, A review of the segmental diameter of the healthy human spinal cord, *Front. Neurol.* **7** (2016) 238.
5. W. Meinhold, D. E. Martinez, J. Oshinski, A.-P. Hu and J. Ueda, A direct drive parallel plane piezoelectric needle positioning robot for mri guided intraspinal injection, *IEEE Trans. Biomed. Eng.* **68**(3) (2020) 807–814.
6. D. E. Martinez, W. Meinhold, J. Oshinski, A.-P. Hu and J. Ueda, Resolution-enhanced mri-guided navigation of spinal cellular injection robot, in *2020 Int. Symp. Medical Robotics (ISMR)* (IEEE, 2020), pp. 83–88.
7. M. Irani and S. Peleg, Motion analysis for image enhancement: Resolution, occlusion, and transparency, *J. Visual Commun. Image Represent.* **4**(4) (1993) 324–335.
8. W. Yang, X. Zhang, Y. Tian, W. Wang, J. Xue and Q. Liao, Deep learning for single image super-resolution: A brief review, *IEEE Trans. Multimedia* **21**(12) (2019) 3106–3121.
9. K. Okarma, M. Tecław and P. Lech, Application of super-resolution algorithms for the navigation of autonomous mobile robots, in *Image Processing & Communications Challenges*, Vol. 6 (Springer, 2015), pp. 145–152.
10. A. Gholipour, J. A. Estroff and S. K. Warfield, Robust super-resolution volume reconstruction from slice acquisitions: application to fetal brain mri, *IEEE Trans. Med. Imag.* **29**(10) (2010) 1739–1758.
11. S. Peled and Y. Yeshurun, Superresolution in mri: application to human white matter fiber tract visualization by diffusion tensor imaging, *Magn. Reson. Med. Official J. Int. Soc. Magn. Reson. Med.* **45** (1) (2001) 29–35.
12. E. Van Reeth, I. W. Tham, C. H. Tan and C. L. Poh, Super-resolution in magnetic resonance imaging: A review, *Concepts Magn. Reson. Part A* **40**(6) (2012) 306–325.
13. M. Hlaváč, A. Knoll, B. Mayer, M. Braun, G. Karpel-Massler, G. Etzrodt-Walter, J. Coburger, C. R. Wirtz and A. Pal'a, Ten years experience with intraoperative mri-assisted transsphenoidal pituitary surgery, *Neurosurg. Focus* **48**(6) (2020) E14.
14. D. B. Comber, E. J. Barth and R. J. Webster, Design and control of an magnetic resonance compatible precision pneumatic active cannula robot, *J. Med. Devices* **8**(1) (2014) 011003.
15. N. Patel, J. Yan, R. Monfaredi, K. Sharma, K. Cleary and I. I. Iordachita, Preclinical evaluation of an integrated robotic system for magnetic resonance imaging guided shoulder arthrography, *J. Med. Imag.* **6**(2) (2019) 025006.
16. N. Hungr, C. Fouard, A. Robert, I. Bricault and P. Cinquin, Interventional radiology robot for CT and MRI guided percutaneous interventions (2011).
17. W. Meinhold, J. Oshinski, A.-P. Hu and J. Ueda, Design and fabrication of an automated spinal precision injection robot, in *BMES Annual Conf.* (2019).
18. H. Greenspan, G. Oz, N. Kiryati and S. Peled, Mri inter-slice reconstruction using super-resolution, *Magn. Reson. Imag.* **20**(5) (2002) 437–446.
19. E. Plenge, D. H. Poot, M. Bernsen, G. Kotek, G. Houston, P. Wielopolski, L. van der Weerd, W. J. Niessen and E. Meijering, Super-resolution methods in mri: can they improve the trade-off between resolution, signal-to-noise ratio, and acquisition time?, *Magn. Reson. Med.* **68**(6) (2012) 1983–1993.
20. D. Thapa, K. Raahemifar, W. R. Bobier and V. Lakshminarayanan, Comparison of super-resolution algorithms applied to retinal images, *J. Biomed. Opt.* **19**(5) (2014) 056002.
21. I. Begin and F. P. Ferrie, Comparison of super-resolution algorithms using image quality measures, in *The 3rd Canadian Conf. Computer and Robot Vision (CRV'06)* (IEEE, 2006), pp. 72–72.
22. V. May, Image Super-Resolution — Iterative Back Projection Algorithm, https://www.mathworks.com/matlabcentral/fileexchange/33839-image-super-resolution-iterative-back-projection-algorithm.
23. K. Chinzei, N. Hata, F. A. Jolesz and R. Kikinis, Mr compatible surgical assist robot: System integration and preliminary feasibility study, in *Int. Conf. Medical Image Computing and Computer-Assisted Intervention* (Springer, 2000), pp. 921–930.
24. A. S. Chaudhari, Z. Fang, F. Kogan, J. Wood, K. J. Stevens, E. K. Gibbons, J. H. Lee, G. E. Gold and B. A. Hargreaves, Super-resolution musculoskeletal mri using deep learning, *Magn. Reson. Med.* **80**(5) (2018) 2139–2154.